RSC Advances

PAPER

View Article Online
View Journal | View Issue

Cite this: *RSC Adv.*, 2025, **15**, 29377

Inhibitory potential of pentagalloyl glucose against efflux pumps in *Staphylococcus aureus*

Kiran Harikumar,[ab] Udisha Singh,[a] Subakamakshi Krishnaswamy Ramaraj,[a] Lakshmi Ajayakumar Rekha,[a] Adyasha Nayak,[a] Poulomi Ghosh,[a] Roshny Prasad,[a] Alwin Philip,[ab] Saloo Sahu[ab] and Shijulal Nelson-Sathi *[ab]

Antibiotic resistance in Gram-positive priority pathogens is mediated by a diverse set of mechanisms such as target protection, antibiotic inactivation, decreased uptake, antibiotic efflux, *etc.* In *Staphylococcus aureus*, efflux pumps of the major facilitator superfamily (MFS) expel various antibiotics and multiple efflux pumps are activated upon antibiotic exposure. Efflux pump inhibitors (EPIs) that can act as antibiotic adjuvants are proposed to be promising solutions to tackle antibiotic resistance. In this study, *in silico* screening of 17 967 phytochemical compounds from Indian medicinal plants (IMPPAT 2.0) against four key MFS efflux pumps activated by fluoroquinolone exposure (NorA, NorB, NorC, and SdrM) followed by *in vitro* validation identified a tannin derivative, pentagalloyl glucose (PGG), as a potential efflux pump inhibitor (EPI) with high binding affinity. Molecular docking scores (≤ -16.383 kcal mol^{-1}) and MM/GBSA binding affinities (≤ -100.62 kcal mol^{-1}) indicate a strong interaction between PGG and its targeted efflux pumps. PGG forms stable interactions *via* hydrogen bonding with key residues of NorA, including GLU222 and ASP307, which are crucial for proton-coupled transport. Likewise, it interacts with essential residues in NorB (SER147, ASN280), NorC (ASN276, LYS398), and SdrM (SER143, GLN283), forming strong hydrogen bonds that contribute to its inhibitory potential. The stability of PGG-bound complexes was confirmed through molecular dynamics simulations over 100 ns in triplicates, along with free energy landscape (FEL) and principal component analysis (PCA). Furthermore, PGG's synergistic action with ciprofloxacin, and effects on *S. aureus* growth dynamics were validated using the checkerboard assay, and time-kill kinetic studies, respectively. Following further structural optimization and *in vivo* studies, PGG can be considered a promising therapeutic candidate against multidrug-resistant *S. aureus* strains.

Received 4th June 2025
Accepted 9th August 2025

DOI: 10.1039/d5ra03958d

rsc.li/rsc-advances

1 Introduction

Antibiotic resistance is one of the top ten global threats as per WHO.[1] This phenomenon directly contributed to an estimated 1.2 million deaths in 2019 alone.[2] Bacteria acquire antibiotic resistance through diverse mechanisms including target protection, target site modification, target bypass, decreased uptake, antibiotic inactivation, active efflux, *etc.*[3] Among these mechanisms, active efflux, mediated by a set of membrane proteins known as efflux pumps, expels antibiotics and other structurally diverse toxic compounds from the cell. This reduces their intracellular concentration, allowing the bacteria to survive.[4] Diverse families of bacterial efflux systems have been reported in literature, including the major facilitator superfamily (MFS), ATP-binding cassette (ABC) family, multidrug and toxic efflux family (MATE), small multidrug resistance (SMR) family and resistance-nodulation-division (RND) family.[5]

Further, in Gram-positive bacteria, particularly the high-priority pathogen *S. aureus*, the MFS has a prevalent set of efflux pumps including the chromosome encoded efflux pumps NorA, NorB, NorC, NorD, SdrM, LmrS, MdeA and Tet38, and the plasmid encoded efflux pumps QacA, QacB, TetK and FexA.[6] Both chromosomally and plasmid-encoded MFS efflux pumps belong to the Drug:H$^+$ Antiporter (DHA) families DHA1 and DHA2. These pumps utilize the proton motive force and operate *via* a rocker-switch mechanism to extrude antibiotics from the bacterial cell.[7] The efficiency of antibiotic efflux by these pumps is attributed to the three-dimensional structural arrangement of amino acid residues within the transmembrane (TM) helices, which form the helical bundles. In the DHA1 family, the helical barrels are composed of twelve transmembrane helices, while in the DHA2 family they consist of fourteen TM helices. In MFS efflux pumps, the TM helices are functionally specialized into distinct categories based on their roles in the pump's mechanism of action. These categories include: cavity helices (TM1, TM4, TM7, and TM10), which are responsible for forming the substrate-binding cavity; rocker helices (TM2, TM5, TM8, and TM11), which facilitate inter-domain conformational changes

[a]*Bioinformatics Laboratory, BRIC-Rajiv Gandhi Centre for Biotechnology, Thiruvananthapuram, 695014, India. E-mail: shijulalns@rgcb.res.in*
[b]*Regional Centre for Biotechnology, Faridabad, Haryana-121001, India*

required for substrate transport; and support helices (TM3, TM6, TM9, and TM12), which do not directly contribute to cavity formation but provide structural stability to the cavity and rocker helices. This stability is achieved through hydrophobic mismatch interactions with the surrounding membrane, ensuring the proper function of the pump.[8,9]

In *S. aureus*, the chromosome-encoded efflux pumps NorA, NorB, NorC, and SdrM exhibit broad substrate specificity compared to plasmid-encoded efflux pumps.[6,10] The wide substrate ranges of these pumps, combined with the extensive distribution of MFS efflux pumps, plays a pivotal role in conferring multidrug resistance in *S. aureus*.[11] Notably, fluoroquinolones, which were one of the traditional therapeutic agents for *S. aureus* infections[12] are a common substrate for NorA, NorB, NorC, and SdrM.[4] Further, it has been reported that in addition to the DHA1 efflux pump NorA, the DHA2 efflux pumps NorB, NorC and SdrM of *S. aureus* are overexpressed upon exposure to fluoroquinolones.[13–15] Since *S. aureus* is acquiring resistance to fluoroquinolones, identifying a fluoroquinolone adjuvant which acts as efflux pump inhibitor (EPI) could reduce the active efflux of these antibiotics leading to bacterial growth inhibition.

Several studies reported the potential of antibiotic adjuvant as EPIs. EPIs can be derived from approved drugs, synthetic and semi-synthetic chemicals, microbial compounds and phytochemicals.[16,17] Felicetti *et al.* designed and synthesized six novel series of quinoline derivatives.[18] Among these, one derivative, namely 2-(3,4-dimethoxyphenyl)quinoline, was found to reduce the ciprofloxacin MIC levels in norA-overexpressing strains of *S. aureus* (SA-K2378 and SA-1199B). Additionally, the compound demonstrated EPI activity at a concentration 50-fold lower than its CC50.[18] Felicetti *et al.* in their study using the SA-1199B strain of *S. aureus*, which overexpresses the norA efflux pump and has a mutation in DNA topoisomerase IV (a fluoroquinolone target), investigated the activity of two methoxy-2-phenylquinoline derivatives.[19] These compounds were tested against several strains, including SA-K2378 (a norA-overexpressing strain), SA-K1902 (a norA-deleted strain), and the wild-type strains ATCC 25923 and SA-1199. Notably, the compounds reduced the minimum inhibitory concentration (MIC) of ciprofloxacin against SA-1199B and revealed an eight-fold difference in ciprofloxacin MIC in the norA-overexpressing strain (SA-K2378) of *S. aureus*. Thus, the study demonstrated that synthetic derivatives act as promising EPIs and potential adjuvants for ciprofloxacin.

Recent studies report phytochemicals such as alkaloids, flavonoids, polyphenols, and phenolic diterpenes as potential efflux pump inhibitors (EPIs), demonstrating their ability to lower the MIC levels of antibiotics in *S. aureus*.[17] Phytochemicals have the advantage of acting as chemical adjuvants in combination with existing antibiotics, effectively inhibiting the efflux system and resulting in synergistic activity.[17] Martin *et al.* reported that coumarin derivatives show promising potential in inhibiting the NorA efflux pump in *S. aureus*.[20] Similarly, Malik *et al.* identified imidazole derivatives as EPIs capable of reducing the MIC of ciprofloxacin, erythromycin, and tetracycline by 128-fold each against the *S. aureus* mutant strains 1199B, XU212, and RN4220, respectively.[21] Additionally, Tintino *et al.* highlighted tannic acid as an effective EPI for the NorA efflux pump in *S. aureus*.[22]

Most studies on EPIs have focused on identifying and validating synthetic and phytochemical-based EPIs targeting the NorA efflux pump, a core gene in *S. aureus*.[23] These studies primarily highlight the potential of such molecules as adjuvants when combined with fluoroquinolone antibiotics. However, current research provides limited insight into the role of these molecules as EPIs for other chromosomally and plasmid-encoded MFS efflux pumps in *S. aureus*. Moreover, an EPI capable of simultaneously targeting multiple MFS efflux pumps associated with fluoroquinolone resistance remains unidentified.

The present study aims to identify phytochemical EPIs that can target multiple MFS efflux pumps in *S. aureus*, including NorA, NorB, NorC, and SdrM which are overexpressed upon fluoroquinolone exposure. Here we performed structure-based virtual screening of 17 967 phytochemicals derived from Indian medicinal plants[24] against NorA, NorB, NorC and SdrM and identified a tannin derivative, pentagalloyl glucose (PGG) as a potential inhibitor. The synergistic activity of PGG is evaluated through checkerboard assays, and its negative impact on *S. aureus* growth is assessed using time-kill kinetics studies. Further *in vivo* validation of PGG could represent a promising therapeutic strategy against multidrug-resistant *S. aureus* strains.

2 Materials and methods

2.1 Computational methods

2.1.1 Sequence analysis. The *S. aureus* reference genome (RefSeq ID: GCF_000013425.1) was downloaded from the National Center for Biotechnology Information (NCBI) RefSeq database.[25] The protein sequences of NorA, NorB, NorC and SdrM were then retrieved from this reference genome. Further, a multiple sequence alignment (MSA) was performed *via* Multiple Alignment using Fast Fourier Transform (MAFFT)[26] with thousand iterations using global optimisation for identifying the sequence conservation among NorA, NorB, NorC and SdrM. EMBOSS Water[27] was used to identify pairwise sequence identities across the above proteins.

2.1.2 Protein structure validation & preparation. High resolution cryo-EM structure of NorA (PDB ID: 7LO8) and X-ray structure of NorC (PDB ID: 7D5P) were downloaded from RCSB Protein Data Bank (RCSB PDB).[28] 3D structures of NorB and SdrM (UniProt ID-Q99S97) were homology-modelled and acquired from AlphaFold[29] respectively. The structure of NorC was used to model NorB *via* the Biologics plugin.[30] Then, structural refinement of NorA, NorC and SdrM was performed by homology modelling.[30] All protein sequences were retrieved from *S. aureus* reference strain NCTC 8325. The modelled protein structures were prepared for further analysis using Protein Preparation Wizard in the Maestro graphical user interface.[31]

2.1.3 Binding site selection & receptor grid generation. Among the five potential binding sites determined for each

efflux pump, NorA, NorB, NorC and SdrM, the one with the highest SiteScore was chosen. Each binding site requires at least 15 site points per reported site and is defined with a cut-off of 4 Å radius from the closest site point.[30] The Receptor Grid Generation panel in the Glide module[32,33] of the Schrödinger Maestro Version 2024-2 was used to create the grid file corresponding to the selected binding pockets of each efflux pump. This grid file was used in the subsequent molecular docking analysis.

2.1.4 Library preparation. A collection of 17 967 phytochemicals was obtained in SMILE format from the IMPPAT 2.0 database (Indian Medicinal Plants, Phytochemistry and Therapeutics).[24] The LigPrep module in the Schrödinger Maestro 2024-2 (ref. 34) was used to prepare the ligands. To account for the flexibility and possible binding modes of the ligands, ring conformations and stereoisomers were created, and the tautomeric and ionisation states of the compounds were broadened to reflect any possible alterations that may occur under physiological settings.

2.1.5 Molecular docking and MM/GBSA. Molecular docking was performed using the Glide module in the Schrödinger's Maestro 2024-2 (ref. 32) with three modes of High-throughput Virtual Screening (HTVS), Standard Precision (SP) and Extra Precision (XP) modes. Top scored compounds from HTVS were subjected to SP and further to XP modes. Molecular Mechanics with Generalized Born Surface Area (MM/GBSA) calculations were carried out for rescoring the docked-ligand postures in the Prime module in the Schrödinger's Maestro 2024-2.[35,36] Additionally, a reported and well-known NorA inhibitor (Piperine) was used as the control for validation. Molecular visualization was carried out using PyMol.[37]

2.1.6 Molecular dynamics simulations. MD simulations using the Desmond module[38] in Schrödinger Maestro (Academic Version 2023-4) were carried out on a time scale of 100 ns in triplicates. The OPLS2005 force field was utilized to accurately depict the intermolecular forces and energy throughout the simulation. Plots and figures were created using Maestro's Simulation interaction diagram tool for data analysis and visualization. The free energy landscape (FEL) of the four efflux pumps NorA, NorB, NorC and SdrM in their native states and when bound to PGG was calculated using the geo_measures v 0.8 plugin on Pymol.[39] The .cms trajectory files from Desmond's output were utilised to plot FEL in Pymol. The Principal Component analysis (PCA) was performed to analyse global movements of the C-alpha atoms of the native proteins and protein–ligand complexes from the trajectories of 100 ns MD simulations, and a covariance matrix was constructed using Schrödinger python script trj_essential_dynamics.py.[40] Membrane model simulations were performed as well on a time scale of 100 ns using POPC (1-palmitoyl-2-oleoylphosphatidylcholine) bilayer in Desmond.[38]

2.2 Experimental methods

2.2.1 Determination of MIC and synergy assay. Broth microdilution method was used to determine the minimum inhibitory concentration (MIC) of the compounds. Serial dilution of ciprofloxacin, PGG, and piperine were performed in 96-well plates. Standardized suspensions of overnight-grown culture of *S. aureus* (ATCC 700698) in TSB (adjusted to OD600 nm of 0.08–0.13) were then added to the plates and incubated at 37 °C for 18 hours. Post 18 hours, MICs were determined by checking the absorbance values (OD600) and confirmed *via* resazurin detection method.[41] MIC assays were performed in triplicates.

The synergistic efficacy of ciprofloxacin with piperine and PGG was determined using a checkerboard assay, following the protocol described by Chandal *et al.* with modifications.[42] The fractional inhibitory concentration index (FICI) was then calculated using the following equation,

$$\mathrm{FICI} = \frac{\mathrm{MIC\ (antibiotic\ in\ the\ presence\ of\ EPI)}}{\mathrm{MIC\ (antibiotic\ alone)}} + \frac{\mathrm{MIC\ (EPI\ in\ the\ presence\ of\ antibiotic)}}{\mathrm{MIC\ (EPI\ alone)}}$$

The FICI values of ≤0.5, 0.5–1, 1–4, and >4 indicate the effect to be synergistic, additive, indifferent, and antagonistic, respectively.

2.2.2 Time-kill kinetics assay. To understand the impact of PGG on the growth rates of fluoroquinolone resistant *S. aureus* (ATCC 700698), time-kill kinetics studies were performed by following the protocol from Adusei *et al.* with modifications.[43] *S. aureus* (ATCC 700698) culture was incubated overnight and was diluted to 0.5 McFarland standard. Different concentrations of ciprofloxacin, PGG, and piperine were administered independently and in combinations. All solutions with *S. aureus* culture were prepared in 15 ml tubes. Post this, 200 μL aliquots including *S. aureus* culture (ATCC 700698) were transferred to 96-well plates for measuring OD600. OD600 readings were obtained from Varioskan Lux multimode microplate reader over a time period of 18 hours.

3 Results and discussion

3.1 Potential binding sites of the targeted MFS efflux pumps

A total of 57, 59, 55 and 45 binding sites residues (SI Table 1) were predicted for the efflux pumps NorA, NorB, NorC and SdrM (Fig. 1B to E) respectively. A pairwise sequence comparison revealed that the similarities between these pumps and binding pockets vary significantly (SI Table 2). MSA of these proteins revealed the binding site residue MET109 (highlighted in yellow) which is conserved across all four efflux pumps, while the remaining residues were not conserved. Between NorB and NorC, 46 identical binding site residues were identified (Fig. 1A). Recently, Li *et al.*[44] showed that, in NorA, the amino acid residues GLU222 in TM7 and ASP307 in TM10 were critical for proton-coupled transport, while Brawley *et al.*[45] demonstrated that the residues PHE16 in TM1 and PHE303 in TM10 were critical for substrate binding. Interestingly, these residues were identified in the predicted binding sites of NorA. Similarly, polar amino acids SER147, ASN217, ASN280 and LYS402 capable of strong interactions were present in the binding sites of NorB. Kumar *et al.*[46] showed that GLY148 in TM5 and LYS398

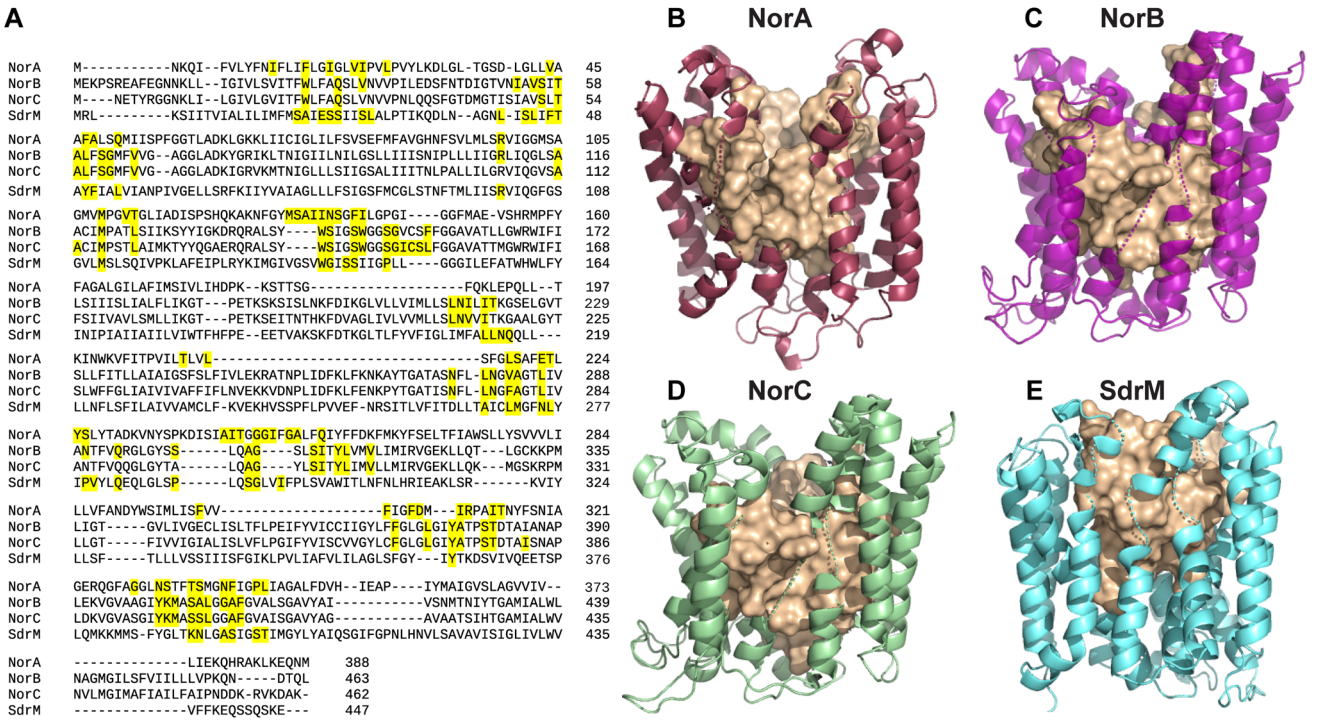

Fig. 1 Predicted binding site residues of the MFS efflux pumps. (A) Multiple sequence alignment of the MFS efflux pumps NorA, NorB, NorC and SdrM. The binding site residues of each efflux pump are highlighted in yellow colour. (B), (C), (D) and (E) are the binding pockets (pale yellow) for the efflux pumps NorA, NorB, NorC and SdrM, respectively.

in TM13 is important for substrate binding and transport in NorC, which is present in the predicted binding site of NorC. Likewise, polar amino acids SER143 and GLN283 were present in the binding sites of SdrM. Thus, a compound that can form stable interactions with the functionally important residues of NorA, NorB, NorC and SdrM in their respective binding sites can potentially disrupt their mechanism.

3.2 Tannin derivative as a potential inhibitor of NorA, NorB, NorC & SdrM

Structure-based virtual screening of 17 967 phytochemicals from the Indian medicinal plants revealed three potential lead compounds that bound simultaneously to the binding pockets of NorA, NorB, NorC and SdrM with high affinities. These three compounds include a tannin derivative, pentagalloyl glucose (PGG) (docking scores ≤ -16.383 kcal mol^{-1} & $\Delta G \leq -100.62$ kcal mol^{-1}) and two flavonoid derivatives, namely, delphinidin-3,5,3′-triglucoside (docking scores ≤ -15.480 kcal mol^{-1} & $\Delta G \leq -70.35$ kcal mol^{-1}) & caffeylmalonylcyanin (docking scores ≤ -14.601 kcal mol^{-1} & $\Delta G \leq -78.04$ kcal mol^{-1}). Among these compounds (SI Table 3), PGG showed the highest binding affinities to NorA, NorB, NorC and SdrM (Table 1).

Additionally, various interactions including H-bonds, hydrophobic interactions and water bridges were identified between PGG and the efflux pumps. We observed that strong interactions of PGG with NorA, NorB, NorC and SdrM were mediated through 5, 9, 6 and 10 H-bonds respectively (SI Table 4). It is reported that amino acid residues SER and ASN are known to form strong H-bonds.[47,48] In NorA, PGG forms 2 H-bonds with ASP307 and a single H-bond with ASN340 (Fig. 2A). Similarly, PGG forms a H-bond with ASN280 of NorB (Fig. 2B) and ASN276 of NorC (Fig. 2C). Interestingly, we observed that these residues were conserved across NorB and NorC (Fig. 1A). Additionally, PGG forms an H-bond with LYS398 of NorC (Fig. 2C), which is important for substrate binding and transport.[46] Also, we observed that a conserved residue, SER143 of NorC and SdrM (Fig. 2D) forms a H-bond with PGG. Therefore, the identified lead compound PGG, can potentially impact the efflux machinery of NorA, NorB, NorC and SdrM by forming strong H-bonds with functionally important residues. Furthermore, it has been reported by Torres-León *et al.* that PGG does not exhibit toxicity to human epithelial and fibroblast cells at concentrations below 50 μM.[49] Similarly, Dettweiler *et al.* conducted a mammalian cytotoxicity assay with human keratinocytes (HaCaTs) and identified an IC_{50} value of 256 μg ml^{-1} for PGG.[50] In a recent study from Marquez *et al.*, PGG was also reported to be well tolerated by human kidney, liver, and epithelial cells having a CC_{50} value of >256 μg ml^{-1}.[51]

3.3 Molecular dynamic simulations using desmond

Molecular dynamics simulations done for 100 ns in triplicates revealed the structural stability of native proteins (NorA, NorB, NorC and SdrM) and protein-PGG complexes. The RMSD plot of the native protein (SI Fig. 1A, C, E and G) was used to understand the structural stability of the native proteins. It was

Table 1 Docking scores and MM/GBSA values of the top-scoring four phytochemicals common to NorA, NorB, NorC and SdrM virtually screened from IMPPAT 2.0. MM/GBSA values are reported for a representative pose of the four protein targets in complex with the ligands after XP docking

		NorA		NorB		NorC		SdrM	
SI No.	Compounds	Docking score	MMGBSA	Docking score	MMGBSA	Docking score	MMGBSA	Docking score	MMGBSA
1	Pentagalloylglucose	−15.323	−89.98	−16.383	−100.62	−13.727	−86.99	−16.298	−80.03
2	Delphinidin 3,5,3′-triglucoside	−15.157	−70.35	−15.480	−68.09	−14.367	−59.46	−13.365	−65.80
3	Caffeylmalonylcyanin	−13.293	−78.04	−13.549	−76.31	−14.164	−73.50	−14.601	−72.15
4	Piperine[a]	−5.460	−48.97	−5.185	−43.05	−5.661	−42.62	−5.699	−38.66

[a] Piperine is the known efflux pump inhibitor used as positive control for the study.

observed that the native proteins were stable and attained equilibrium after 15 ns, 6 ns, 9 ns and 3 ns at RMSDs ranging between 4 to 4.8 Å, 3.7 to 4.1 Å, 4.3 to 5.0 Å and 3.4 to 4.2 Å respectively. Similarly, the RMSD plot for the NorA-PGG, NorB-PGG, NorC-PGG and SdrM-PGG demonstrate a stable interaction pattern between the protein and the ligand. From the RMSD of the NorA-PGG complex (Fig. 3A) it was observed that the complex is attaining equilibrium after 20 ns, with an RMSD ranging between 2.7 and 4.0 Å for both NorA and PGG.

Additionally, the NorA-PGG complex (Fig. 3B) shows a lower RMSF value for the interacting amino acid residues, indicating high rigidity, whereas structurally flexible loop regions exhibited higher RMSF values. A similar pattern is observed in the loop regions of the native NorA with a high RMSF value whereas the interacting residues show a low RMSF profile (SI Fig. 1B). Moreover, the interaction plot for the NorA-PGG complex highlighted the presence of hydrogen bonds, water bridges, and hydrophobic interactions. The majority of interactions were contributed *via* H-bond and water bridges involving GLN51, SER133, ASN137, THR223, ASP307, THR336, and ASN340. Interestingly, residues ASN137, PHE140, GLU222, and ASP307 were previously identified as key residues for substrate binding

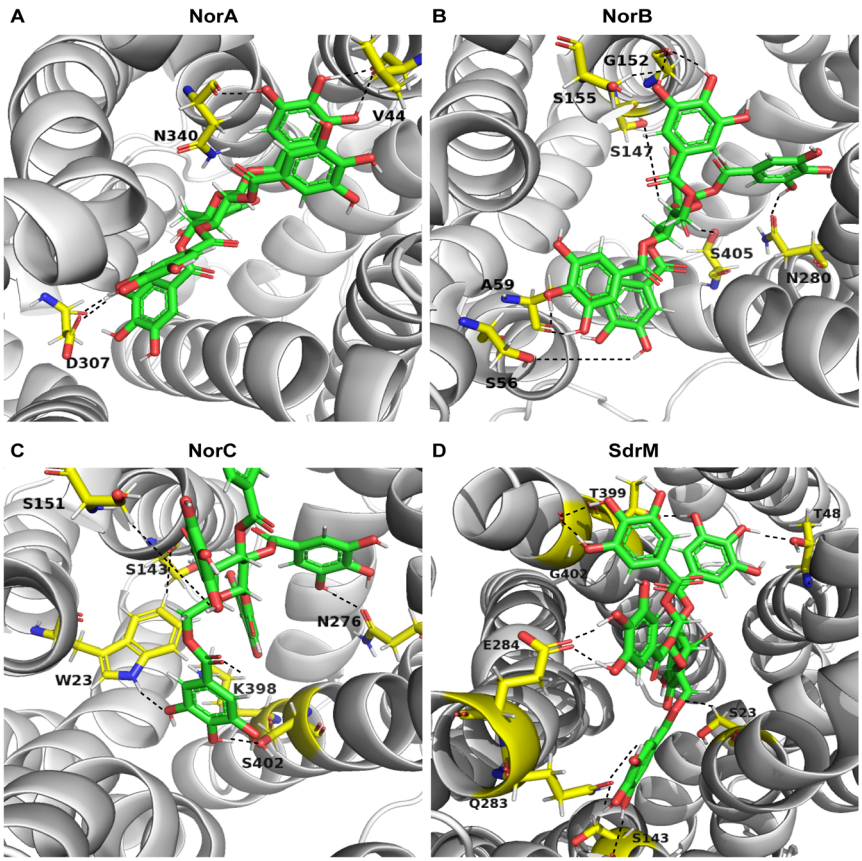

Fig. 2 Hydrogen bond interaction between pentagalloyl glucose (PGG) and efflux pumps. Interaction diagrams of PGG with (A) NorA, (B) NorB, (C) NorC and (D) SdrM. The Carbon backbone of PGG (green) and the amino acid residues (yellow) are marked as single letter codes followed by position. Hydrogen bonds between the amino acid residues and pentagalloyl glucose are represented as black dashes.

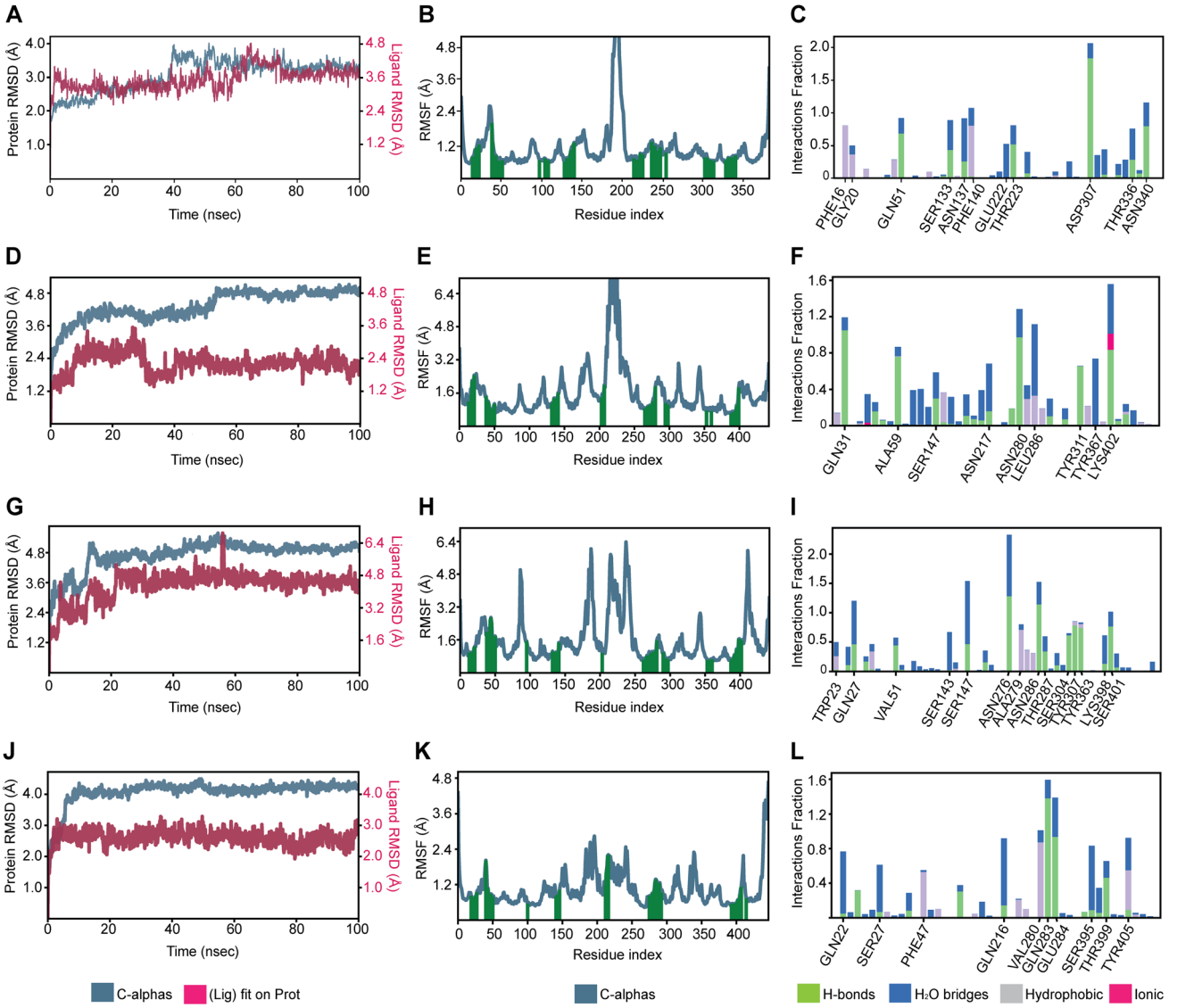

Fig. 3 Molecular dynamic simulations of the protein–ligand complexes. (A) RMSD, (B) RMSF and (C) interaction plots for NorA-PGG complex. (D) RMSD, (E) RMSF and (F) interaction plots for NorB-PGG complex. (G) RMSD, (H) RMSF and (I) interaction plots for NorC-PGG complex. (J) RMSD, (K) RMSF and (L) interaction plots for SdrM-PGG complex. In interaction plots, the *x*-axis was labelled with residues with an interaction fraction greater than 0.5.

and proton-coupled substrate transport in NorA. It has been highlighted by Li *et al.* that protonation–deprotonation of both GLU222, ASP307 are crucial for conformational changes of NorA during substrate transport in *S. aureus*.[44] By binding to these residues, PGG can interfere with this protonation–deprotonation ensuring that the outward-open conformation of NorA does not interchange between occluded or inward-open states.

Furthermore, the protein RMSD plots for NorB-PGG (Fig. 3D), NorC-PGG (Fig. 3G) and SdrM-PGG (Fig. 3J) complex demonstrate a stable interaction pattern. In all three cases, the ligand RMSD remains lower than the protein RMSD throughout the simulation, indicating that the ligand undergoes minimal conformational changes and remains stably positioned within the binding site. Additionally, the RMSF plots for the NorB-PGG (Fig. 3E), NorC-PGG (Fig. 3H), and SdrM-PGG (Fig. 3K) complexes exhibit a similar trend to that observed for the NorA-PGG complex, reinforcing the structural stability of these systems. Interestingly, these observations were also in line with the RMSD (SI Fig. 1C, E and G) and the RMSF (SI Fig. 1D, F and H) values of the native proteins NorB, NorC and SdrM respectively.

Moreover, the major fraction of the stability of these protein-PGG complexes is contributed *via* the hydrogen bonds and water bridges. GLN31, ALA59, SER147, ASN217, TYR311 and LYS402 were the key residues contributing to these interactions in NorB-PGG complex while TRP23, GLN27, VAL51, SER143, SER147, ASN276, ASN286, THR287, SER304, TYR307, TYR363, LYS398 and SER401 contributes to the stability of NorC-PGG complex. PGG can potentially affect the protonation of LYS398 in NorC, which has been indicated by Kumar *et al.* to be

involved in substrate recognition, disrupting its transport.[46] Similarly, the residues GLN22, SER27, PHE47, GLN216, GLN283, GLU283, SER395 and THR399 majorly contribute to the stability of the SdrM-PGG complex.

To gain further insights into the conformational stability of protein-PGG complexes when embedded into a biological membrane, POPC (1-palmitoyl-2-oleoylphosphatidylcholine) membrane-model simulations were performed. The RMSD profiles (SI Fig. 2) revealed high stability for protein-PGG complexes indicating that PGG can act as a potential inhibitor of NorA, NorB, NorC and SdrM in *S. aureus*.

3.4 Free energy landscape for MFS targets complexed with PGG

The free energy landscape (FEL) of NorA-PGG, NorB-PGG, NorC-PGG and SdrM-PGG complex (Fig. 4A–D) were compared with the native proteins (SI Fig. 3) to obtain key insights into the conformational states and stability of the PGG bound state of the proteins. The native NorA exhibits a stable conformation, characterized by local minima for RMSD and radius of gyration (RG) in the ranges of 0.4–0.5 nm and 2.02–2.04 nm, respectively. This is represented by the blue region (indicating minimum Gibbs free energy) in the contour plot of the FEL, mapped onto the RMSD *versus* RG plane (SI Fig. 3A). In comparison, the FEL for NorA-PGG complex (Fig. 4A) shows two local minima in a range between 0.25–0.4 nm and 2.10–2.14 nm for RMSD and RG respectively. This indicates the possibility of two stable conformations. However, the local minima for Gibbs free energy, RMSD, and RG suggest that both these conformations were thermodynamically stable in comparison to the local minima of the native NorA.

Similarly, the FEL of the NorB-PGG complex also exhibits two thermodynamically stable conformations within the minimal Gibbs free energy region on the contour plot (Fig. 4B), with

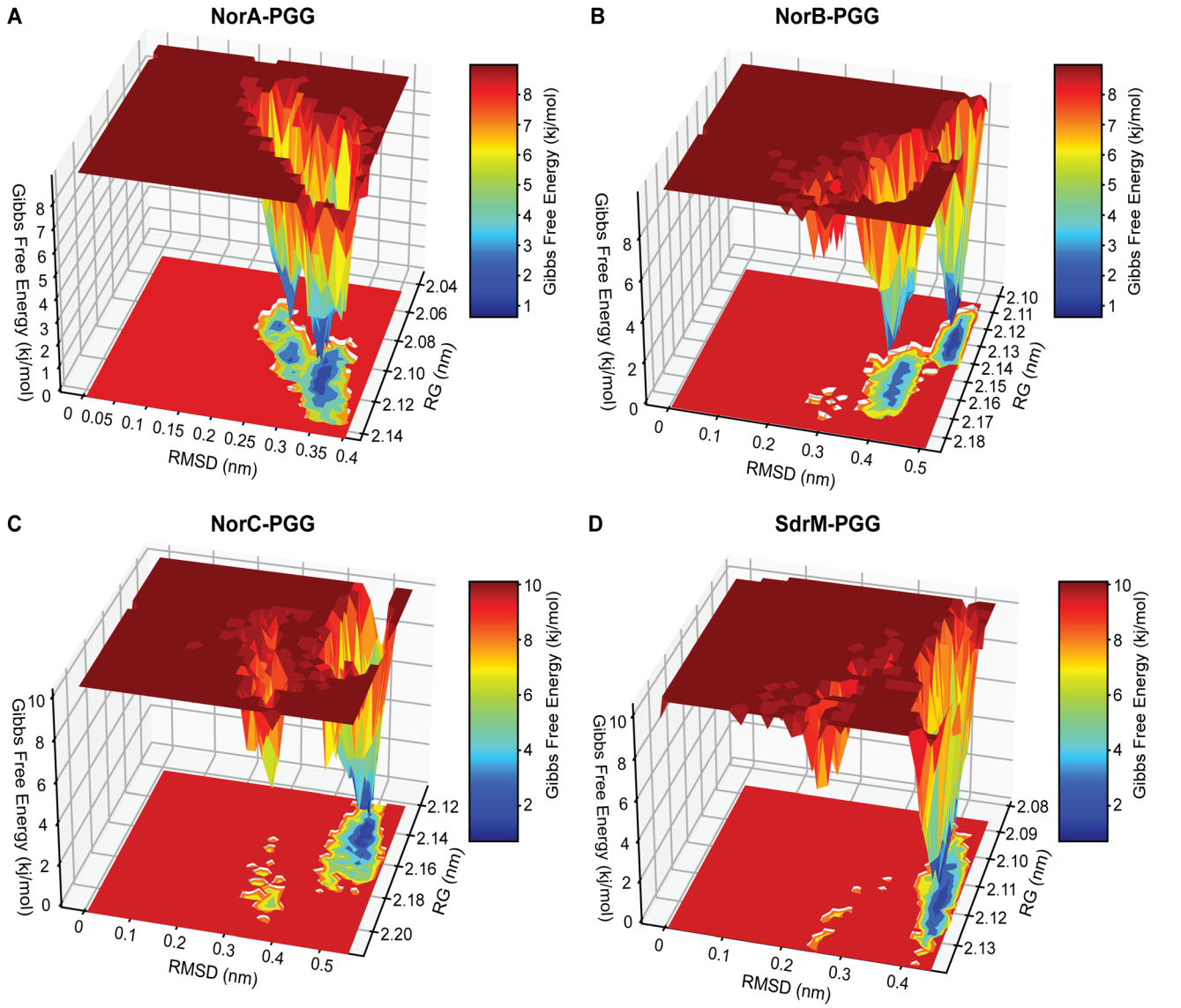

Fig. 4 Free energy landscape of the NorA-PGG (A), NorB-PGG (B), NorC-PGG (C) and SdrM-PGG (D). The Gibbs free energy is plotted against the RMSD and radius of gyration (RG). The colour bar displays the Gibbs free energy values.

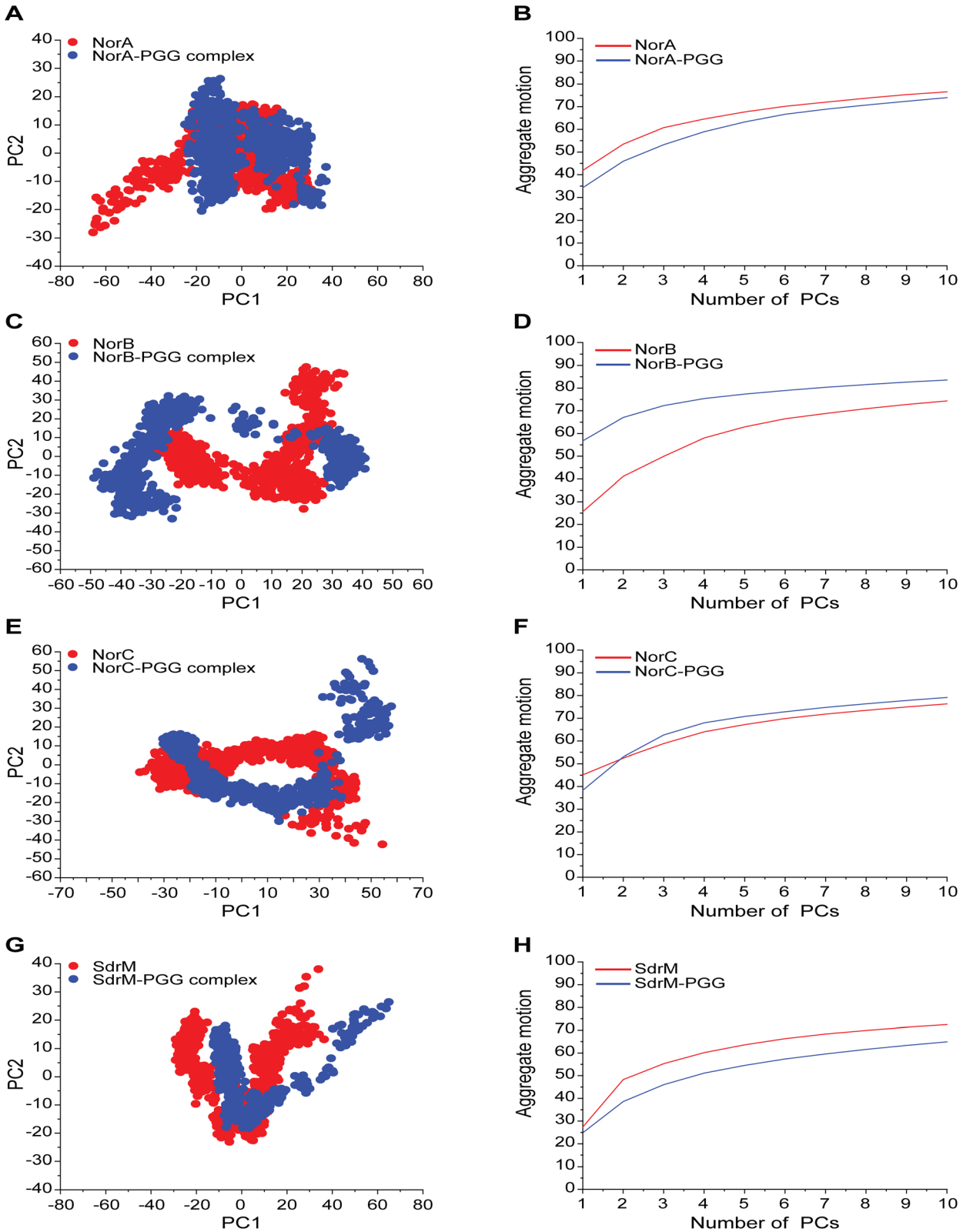

Fig. 5 Principal component analysis of trajectory motions of native proteins and protein-pentagalloyl glucose (PGG) complexes. (A) PCA score plot for the NorA *versus* the NorA-PGG complex along the PC1–PC2 axis. (B) Aggregate motion explained by the 10 principal components (PCs) for NorA *versus* NorA-PGG complex. (C) PCA score plot for NorB *versus* the NorB-PGG complex along the PC1–PC2 axis. (D) Aggregate motion explained by the 10 PCs for NorB *versus* NorB-PGG complex. (E) PCA score plot for NorC *versus* the NorC-PGG complex along the PC1–PC2 axis. (F) Aggregate motion explained by the 10 PCs for NorC *versus* NorC-PGG complex. (G) PCA score plot for SdrM *versus* the SdrM-PGG complex along the PC1–PC2 axis. (H) Aggregate motion explained by the 10 PCs for SdrM *versus* SdrM-PGG complex.

RMSD values ranging from 0.4 to 0.5 nm and RG values ranging from 2.11 to 2.17 nm. These local minima were comparatively lower than those observed in the FEL of the NorB protein (SI Fig. 3B), suggesting the structural stability of the NorB-PGG complex. Furthermore, the FELs of the NorC-PGG (Fig. 4C) and SdrM-PGG (Fig. 4D) complexes each exhibit a single local minimum in the RMSD *versus* RG plane. The local minimum for NorC-PGG is observed at RMSD values between 0.5 and 0.55 nm and RG values between 2.14 and 2.16 nm, while the local minimum for SdrM-PGG is found at RMSD values between 0.4 and 0.45 nm and RG values between 2.10 and 2.13 nm. These observations align with the local minima observed in the FELs of NorC (SI Fig. 3C) and SdrM (SI Fig. 3D), further validating the stable conformations of both the NorC-PGG and SdrM-PGG complexes.

3.5 Principal component analysis for the targets complexed with PGG

Principal component analysis (PCA) was used to understand the conformational changes exhibited by the native proteins and protein-PGG complexes during the simulation period (Fig. 5). The first two principal components (PCs) accounted for ≥41.1% variation across native proteins and ≥38.6% motion across the protein-PGG complexes. In comparison to the native proteins, the protein-PGG complexes showed minimal conformational changes (Fig. 5). However, for NorB (Fig. 5C and D), a significant conformational difference was observed between native and PGG-bound states. In the native state of NorB, an aggregate motion of 41.1% was explained by the first two PCs which increased to 67.05% when bound to PGG. NorA, NorC and SdrM when bound to PGG had 46%, 53% and 38.6% of aggregate motion explained by the first two PCs while their native states had 53.5%, 52.5% and 48.3% motion explained by the same PCs (Fig. 5). Thus, the conformational stability of NorA, NorB, NorC and SdrM during the MD simulation was outlined by PCA, further indicating that PGG can potentially inhibit these four efflux pumps.

3.6 Minimum inhibitory concentration and the synergistic effect of PGG with ciprofloxacin

The individual MICs of ciprofloxacin, piperine, PGG, and the combinations of piperine and PGG with ciprofloxacin was determined using the *S. aureus* ATCC 700698 strain, which is resistant to ciprofloxacin (Table 2). Piperine, being a known NorA inhibitor[52] was used as a positive control for the study. The independent MIC values for ciprofloxacin (125 μg ml^{-1}), piperine (250 μg ml^{-1}) and PGG (250 μg ml^{-1}) were determined. However, when piperine and PGG were tested in combination with ciprofloxacin, they demonstrated additive and synergistic effects, with FICI values of 0.7 and 0.45, respectively. An FICI value less than 0.5 indicates synergy, meaning the combination of drugs works better together than each drug alone, enhancing each other's effectiveness. An FICI between 0.5 and 1.0 indicates an additive effect, where the combination of drugs works similarly to the sum of the individual effects. In the case of synergy, an MIC of 25 μg ml^{-1} for ciprofloxacin and 62.5 μg ml^{-1} for PGG was identified, which represents a four-fold reduction in concentration compared to the independent MIC of PGG. Additionally, the MIC of PGG in combination with ciprofloxacin was lower than the MIC of piperine (125 μg ml^{-1}) in combination with ciprofloxacin, although the ciprofloxacin concentration remained similar (25 μg ml^{-1}) in both cases. Thus, a lower concentration of PGG in combination with ciprofloxacin was more effective in inhibiting bacterial growth than piperine in combination with ciprofloxacin (Table 2).

3.7 Time-kill kinetics of *S. aureus*

Time-kill kinetics assay was performed to determine the growth inhibitory effect of PGG against *S. aureus* (ATCC 700698) (Fig. 6). PGG (62.5 μg ml^{-1}) in combination with ciprofloxacin (25 μg ml^{-1}) inhibited the *S. aureus* growth in a similar manner as observed for ciprofloxacin MIC (125 μg ml^{-1}). In contrast, PGG (62.5 μg ml^{-1}) and ciprofloxacin (25 μg ml^{-1}) when administered independently resulted in bacterial growth, confirming the synergistic effect of PGG-ciprofloxacin combination against *S. aureus* (ATCC 700698). Additionally, PGG showed better *S. aureus* growth inhibition when compared to piperine (a known NorA inhibitor). Piperine is reported to have OD_{600} values >0.1 (ref. 53) which contribute to the increased OD at zeroth and second hour, where bacterial growth is not noticeable (Fig. 6). This was verified by recording the OD_{600} values of piperine and piperine–ciprofloxacin combination in the absence of *S. aureus* cultures (SI Table 5). Piperine inhibited *S. aureus* growth at a high concentration (125 μg ml^{-1}) when combined with ciprofloxacin (25 μg ml^{-1}) and did not exhibit considerable effect when administered independently. A steady increase in *S. aureus* growth was observed when exposed to 25 μg ml^{-1} of ciprofloxacin with notable growth occurring after eight hours. This suggests the initial activity of ciprofloxacin against *S. aureus* which gradually decreases over time leading to bacterial growth (Fig. 6).

Table 2 MIC values obtained from checkerboard assay of ciprofloxacin in combination with (a) pentagalloyl glucose (PGG) and (b) piperine performed for *S. aureus* (ATCC 700698)

Combination	MIC^{alone} (μg ml^{-1})	MIC^{comb} (μg ml^{-1})	FIC (MIC^{comb}/MIC^{alone})	FICI	Effect
Ciprofloxacin	125	25	0.2	0.45	Synergy
PGG	250	62.5	0.25		
Ciprofloxacin	125	25	0.2	0.7	Additive
Piperine	250	125	0.5		

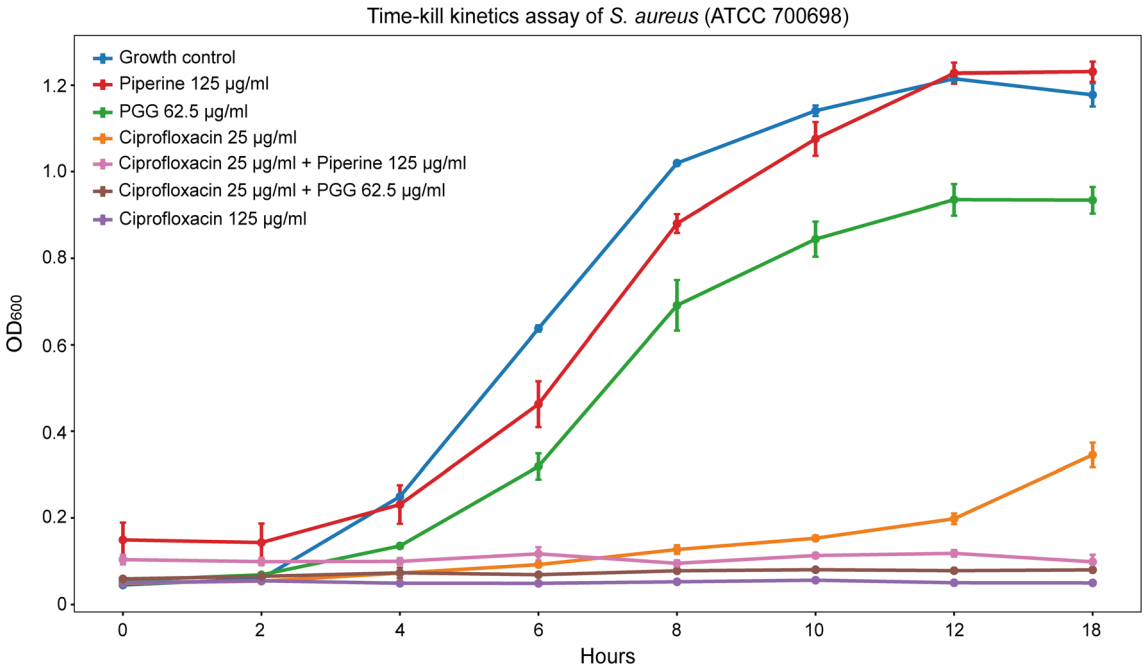

Fig. 6 Time-kill assay depicting *S. aureus* growth on exposure to ciprofloxacin, piperine, PGG when administered independently and in combination. The concentrations taken for PGG (62.5 µg ml^{-1}) and piperine (125 µg ml^{-1}) are with respect to their synergistic and additive effects respectively when combined with ciprofloxacin. Bacterial growth was measured in terms of absorbance at 600 nm (OD_{600}) and readings were taken for 18 hours. The experiment was conducted in triplicates and data are expressed as mean ± standard deviation.

4 Conclusions

Our *in silico* and *in vitro* study identified PGG as a potential inhibitor of the MFS efflux pumps NorA, NorB, NorC and SdrM in multi-drug resistant *S. aureus*. PGG's influence on the *S. aureus* growth dynamics were revealed by time-kill kinetics assay. Checkerboard assays revealed that PGG exhibited phytochemical synergy in combination with ciprofloxacin and restored the ciprofloxacin activity in *S. aureus*. Therefore, our study reveals PGG as a promising candidate for combating clinically relevant *S. aureus* strains. Further, the work underlines the importance of exploring plant-derived compounds as an avenue for overcoming antibiotic resistance caused by bacterial pathogens.

Author contributions

Conceptualization, S. N.-S.; methodology, S. N.-S., K. H., U. S., S. K. R., S. S.; investigation, K. H., U. S., S. K. R., L. A. R., A. N., P. G., A. P., S. S.; validation, K. H., U. S., S. K. R., S. S.; data curation, K. H. and U. S.; writing-original draft, S. N.-S., K. H., U. S., L. A. R., R. P.; supervision, S. N.-S.; and writing – review and editing S. N.-S., K. H.; all authors have read and agreed to the submitted version of the manuscript.

Conflicts of interest

There are no conflicts to declare.

Data availability

The reference genome of *S. aureus* is publicly available in NCBI Datasets at **https://www.ncbi.nlm.nih.gov/datasets/genome/GCF_000013425.1/**with RefSeq ID: GCF_000013425.1. The protein structures are publicly available in RCSB PDB for NorA at **https://www.rcsb.org/structure/7LO8** with PDB ID: 7LO8 and NorC at **https://www.rcsb.org/structure/7D5P** with PDB ID: 7D5P. The protein structure of SdrM is publicly available in AlphaFold at **https://alphafold.com/entry/Q99S97** with UniProt ID: Q99S97. The phytochemical ligand library is publicly available in IMPPAT 2.0 database at **https://cb.imsc.res.in/imppat/home**. The utility script trj_essential_dynamics.py is contained within the Schrödinger suite.

Acknowledgements

The authors wish to thank Prof. Chandrabhas Narayana, the Director, BRIC-Rajiv Gandhi Centre for Biotechnology for providing intramural support and the Bioinformatics Facility for providing the necessary computational infrastructure. The authors would like to acknowledge Dr Dileep Vasudevan and Dr Kathiresan Natarajan at BRIC-Rajiv Gandhi Centre for Biotechnology for their active discussion. Innovation in Science pursuit for Inspired Research from the Department of Science and Technology (DST-INSPIRE Fellowship), Ministry of Science and Technology, India, funded K.H (DST/INSPIRE/03/2023/000917).

References

1 T. R. Walsh, A. C. Gales, R. Laxminarayan and P. C. Dodd, *PLoS Med.*, 2023, e1004264, DOI: 10.1371/journal.pmed.1004264.
2 C. J. L. Murray, K. S. Ikuta, F. Sharara, L. Swetschinski, G. R. Aguilar, A. Gray, *et al.*, *Lancet*, 2022, **399**, 629–655.
3 E. M. Darby, E. Trampari, P. Siasat, M. S. Gaya, I. Alav, M. A. Webber, *et al.*, *Nat. Rev. Microbiol.*, 2022, **21**, 280–295.
4 M. Kumawat, B. Nabi, M. Daswani, I. Viquar, N. Pal, P. Sharma, *et al.*, *Microb. Pathog.*, 2023, **181**, 106182.
5 M. A. Webber and L. J. V. Piddock, *J. Antimicrob. Chemother.*, 2003, **51**, 9–11.
6 S. Hernando-Amado, P. Blanco, M. Alcalde-Rico, F. Corona, J. A. Reales-Calderón, M. B. Sánchez, *et al.*, *Drug Resistance Updates*, 2016, **28**, 13–27.
7 D. Du, H. W. Van Veen, S. Murakami, K. M. Pos and B. F. Luisi, *Curr. Opin. Struct. Biol.*, 2015, **33**, 76–91.
8 D. Drew, R. A. North, K. Nagarathinam and M. Tanabe, *Chem. Rev.*, 2021, **121**, 5289–5335.
9 X. C. Zhang, Y. Zhao, J. Heng and D. Jiang, *Protein Sci.*, 2015, **24**, 1560–1579.
10 B. D. Schindler and G. W. Kaatz, *Drug Resistance Updates*, 2016, **27**, 1–13.
11 J. Stephen, F. Salam, M. Lekshmi, S. H. Kumar and M. F. Varela, *Antibiotics*, 2023, 343, DOI: 10.3390/antibiotics12020343.
12 A. Shariati, M. Arshadi, M. A. Khosrojerdi, M. Abedinzadeh, M. Ganjalishahi, A. Maleki, *et al.*, *Front. Public Health*, 2022, **10**, 1025633.
13 A. Fàbrega, S. Madurga, E. Giralt and J. Vila, *Microb. Biotechnol.*, 2008, **2**, 40–61.
14 A. Papkou, J. Hedge, N. Kapel, B. Young and R. C. MacLean, *Nat. Commun.*, 2020, 3970, DOI: 10.1038/s41467-020-17735-y.
15 T. Q. Huynh, V. N. Tran, V. C. Thai, H. A. Nguyen, N. T. G. Nguyen, M. K. Tran, *et al.*, *PLoS One*, 2023, 0287973, DOI: 10.1371/journal.pone.0287973.
16 S. A. A. M. Abdel-Karim, A. M. A. El-Ganiny, M. A. El-Sayed and H. A. A. Abbas, *PLoS One*, 2022, e0272417, DOI: 10.1371/journal.pone.0272417.
17 A. Sharma, V. K. Gupta and R. Pathania, *Indian J. Med. Res.*, 2019, **149**, 129–145.
18 T. Felicetti, R. Cannalire, M. S. Burali, S. Massari, G. Manfroni, M. L. Barreca, *et al.*, *ChemMedChem*, 2017, **12**, 1293–1302.
19 T. Felicetti, R. Cannalire, M. G. Nizi, O. Tabarrini, S. Massari, M. L. Barreca, *et al.*, *Eur. J. Med. Chem.*, 2018, **155**, 428–433.
20 A. L. A. R. Martin, R. L. S. Pereira, J. E. Rocha, P. A. M. Farias, T. S. Freitas, F. R. De Lemos Caldas, *et al.*, *Microb. Pathog.*, 2024, **190**, 106608.
21 A. A. Malik, N. A. Dangroo, P. Kaur, S. Attery, M. A. Rather, A. Khan, *et al.*, *Microb. Pathog.*, 2024, **190**, 106627.
22 S. R. Tintino, P. Wilairatana, V. C. A. De Souza, J. M. A. Da Silva, P. S. Pereira, C. D. De Morais Oliveira-Tintino, *et al.*, *Sci. Rep.*, 2023, 17394, DOI: 10.1038/s41598-023-43038-5.
23 S. S. Costa, B. Sobkowiak, R. Parreira, J. D. Edgeworth, M. Viveiros, T. G. Clark, *et al.*, *Front. Genet.*, 2019, 710, DOI: 10.3389/fgene.2018.00710.
24 R. P. Vivek-Ananth, K. Mohanraj, A. K. Sahoo and A. Samal, *ACS Omega*, 2023, **8**, 8827–8845.
25 E. W. Sayers, E. E. Bolton, J. R. Brister, K. Canese, J. Chan, D. C. Comeau, *et al.*, *Nucleic Acids Res.*, 2021, **50**, D20–D26.
26 K. Katoh, *Nucleic Acids Res.*, 2002, **30**, 3059–3066.
27 P. Rice, I. Longden and A. Bleasby, *Trends Genet.*, 2000, **16**, 276–277.
28 H. M. Berman, *Nucleic Acids Res.*, 2000, **28**, 235–242.
29 J. Jumper, R. Evans, A. Pritzel, T. Green, M. Figurnov, O. Ronneberger, *et al.*, *Nature*, 2021, **596**, 583–589.
30 *Schrödinger Release 2024-2*, https://www.schrodinger.com/life-science/download/release-notes/release-2024-2/, accessed June 2025.
31 G. M. Sastry, M. Adzhigirey, T. Day, R. Annabhimoju and W. Sherman, *J. Comput.-Aided Mol. Des.*, 2013, **27**, 221–234.
32 Y. Yang, K. Yao, M. P. Repasky, K. Leswing, R. Abel, B. K. Shoichet, *et al.*, *J. Chem. Theory Comput.*, 2021, **17**, 7106–7119.
33 R. A. Friesner, J. L. Banks, R. B. Murphy, T. A. Halgren, J. J. Klicic, D. T. Mainz, *et al.*, *J. Med. Chem.*, 2004, **47**, 1739–1749.
34 *Schrödinger Release 2024-2*, https://www.schrodinger.com/life-science/download/release-notes/release-2024-2/, accessed June 2025.
35 M. P. Jacobson, R. A. Friesner, Z. Xiang and B. Honig, *J. Mol. Biol.*, 2002, **320**, 597–608.
36 M. P. Jacobson, D. L. Pincus, C. S. Rapp, T. J. F. Day, B. Honig, D. E. Shaw, *et al.*, *Proteins:Struct., Funct., Bioinf.*, 2004, **55**, 351–367.
37 *The PyMOL Molecular Graphics System*, https://www.pymol.org/support.html?#citing, accessed June 2025.
38 K. J. Bowers, D. E. Chow, H. Xu, R. O. Dror, M. P. Eastwood, B. A. Gregersen, *et al.*, *SC '06: Proceedings of the 2006 ACM/IEEE Conference on Supercomputing*, IEEE, Florida, 2006.
39 L. P. Kagami, G. M. D. Neves, L. F. S. M. Timmers, R. A. Caceres and V. L. Eifler-Lima, *Comput. Biol. Chem.*, 2020, **87**, 107322.
40 *Working with Trajectories*, https://learn.schrodinger.com/public/python_api/2022-3/trajectories.html, accessed June 2025.
41 M. Elshikh, S. Ahmed, S. Funston, P. Dunlop, M. McGaw, R. Marchant, *et al.*, *Biotechnol. Lett.*, 2016, **38**, 1015–1019.
42 N. Chandal, R. Tambat, R. Kalia, G. Kumar, N. Mahey, S. Jachak, *et al.*, *Microbiol. Spectrum*, 2023, **11**, e04876.
43 E. B. A. Adusei, R. K. Adosraku, J. Oppong-Kyekyeku, C. D. K. Amengor and Y. Jibira, *J. Trop. Med.*, 2019, **2019**, 1250645.
44 J. Li, Y. Li, A. Koide, H. Kuang, V. J. Torres, S. Koide, *et al.*, *Nat. Commun.*, 2024, 4494, DOI: 10.1038/s41467-024-48759-3.
45 D. N. Brawley, D. B. Sauer, J. Li, X. Zheng, A. Koide, G. S. Jedhe, *et al.*, *Nat. Chem. Biol.*, 2022, **18**, 706–712.

46 S. Kumar, A. Athreya, A. Gulati, R. M. Nair, I. Mahendran, R. Ranjan, *et al.*, *Commun. Biol.*, 2021, 836, DOI: 10.1038/s42003-021-02357-x.
47 G. Liapakis, J. A. Ballesteros, S. Papachristou, W. C. Chan, X. Chen and J. A. Javitch, *J. Biol. Chem.*, 2000, **275**, 37779–37788.
48 C. X. Weichenberger and M. J. Sippl, *Structure*, 2006, **14**, 967–972.
49 C. Torres-León, J. Ventura-Sobrevilla, L. Serna-Cock, J. A. Ascacio-Valdés, J. Contreras-Esquivel and C. N. Aguilar, *J. Funct. Foods*, 2017, **37**, 176–189.
50 M. Dettweiler, L. Marquez, M. Lin, A. M. Sweeney-Jones, B. K. Chhetri, D. V. Zurawski, *et al.*, *Sci. Rep.*, 2020, **10**, 15340.
51 L. Marquez, Y. Lee, D. Duncan, L. Whitesell, L. E. Cowen and C. Quave, *ACS Infect. Dis.*, 2023, **9**, 1685–1694.
52 I. A. Khan, Z. M. Mirza, A. Kumar, V. Verma and G. N. Qazi, *Antimicrob. Agents Chemother.*, 2006, **50**, 810–812.
53 C. P. Bravo-Chaucanés, L. C. Chitiva, Y. Vargas-Casanova, V. Diaz-Santoyo, A. X. Hernández, G. M. Costa, *et al.*, *Biomolecules*, 2023, **13**, 1729.